Catalysis Today 231 (2014) 135–144

Contents lists available at ScienceDirect

Catalysis Today

journal homepage: www.elsevier.com/locate/cattod

NO_x storage and reduction pathways on zirconia and titania functionalized binary and ternary oxides as NO_x storage and reduction (NSR) systems

Zafer Say, Merve Tohumeken, Emrah Ozensoy*

Department of Chemistry, Bilkent University, 06800 Ankara, Turkey

ARTICLE INFO

Article history:
Received 22 October 2013
Received in revised form
17 December 2013
Accepted 19 December 2013
Available online 28 January 2014

Keywords:
Zirconia
Titania
Pt
NO_x
LNT
NSR

ABSTRACT

Binary and ternary oxide materials, ZrO_2/TiO_2 (ZT) and $Al_2O_3/ZrO_2/TiO_2$ (AZT), as well as their Pt-functionalized counterparts were synthesized and characterized via XRD, Raman spectroscopy, BET, in situ FTIR and TPD techniques. In the ZT system, a strong interaction between TiO_2 and ZrO_2 domains at high temperatures (>973 K) resulted in the formation of a low specific surface area (i.e. 26 m^2/g at 973 K) ZT material containing a highly ordered crystalline $ZrTiO_4$ phase. Incorporation of Al_2O_3 in the AZT structure renders the material highly resilient toward crystallization and ordering. Alumina acts as a diffusion barrier in the AZT structure, preventing the formation of $ZrTiO_4$ and leading to a high specific surface area (i.e. 264 m^2/g at 973 K). NO_x adsorption on the AZT system was found to be significantly greater than that of ZT, due to almost ten-fold greater SSA of the former surface. While Pt incorporation did not alter the type of the adsorbed nitrate species, it significantly boosted the NO_x adsorption on both Pt/ZT and Pt/AZT systems. Thermal stability of nitrates was higher on the AZT compared to ZT, most likely due to the defective structure and the presence of coordinatively unsaturated sites on the former surface. Pt sites also facilitate the decomposition of nitrates in the absence of an external reducing agent by shifting the decomposition temperatures to lower values. Presence of Pt also enhances partial/complete NO_x reduction in the absence of an external reducing agent and the formation of N_2 and N_2O. In the presence of H_2(g), reduction of surface nitrates was completed at 623 K on ZT, while this was achieved at 723 K for AZT. Nitrate reduction over Pt/ZT and Pt/AZT via H_2(g) under mild conditions initially leads to conversion of bridging nitrates into monodentate nitrates/nitrites and the formation of surface —OH and —NH_x functionalities. N_2O(g) was also continuously generated during the reduction process as an intermediate/byproduct.

1. Introduction

Automobile industry has been forced by new, more stringent regulations to invent novel technologies for the elimination of the environmental impact of exhaust emissions. Since three-way catalysts are not efficient under lean conditions, NO_x storage and reduction (NSR) catalysts have been developed by Toyota Motor Company as a promising after-treatment process [1,2]. The operational principle of NSR catalysts relies on the fact that NO(g) is initially oxidized to NO_2(g) on the precious metal site under lean conditions followed by storage in the form of nitrites and nitrates on a NO_x storage domain such as BaO or K_2O [3–8]. Finally, stored NO_x species are reduced to N_2(g) in the rich operational cycle [3]. For a detailed discussion the NO_x storage and reduction technology, reader is referred to two comprehensive reviews by Roy et al. [3] and Epling et al. [4].

However, NSR materials have two major drawbacks namely, sulfur poisoning [9,10] and thermal aging [5,11,12]. Senturk et al. investigated the effect of TiO_2 promotion on the BaO/Al_2O_3 binary oxide and demonstrated that the sulfur uptake and release properties of the TiO_2-promoted BaO/Al_2O_3 materials were significantly enhanced [13]. Matsumoto et al. [14] also reported that TiO_2 could be used as a promoter against sulfur poisoning due to its high acidity. However, it has been also reported that titania can readily lose its functionality due to thermal deterioration at high temperatures and various solid-phase reactions between NO_x storage domains, promoters and the support material [11,12,15]. Therefore, ZrO_2 is typically used together with TiO_2 in an attempt to stabilize the titania component [16,17]. Another critical factor that favors the usage of ZrO_2/TiO_2 as a mixed metal oxide component is its higher surface acidity as compared to either ZrO_2 or TiO_2, alone [18,19].

ZrO_2/TiO_2 and $Al_2O_3/ZrO_2/TiO_2$ mixed oxides have recently been thoroughly studied with a particular emphasis on the sulfur

* Corresponding author. Tel.: +90 3122902121.
E-mail address: ozensoy@fen.bilkent.edu.tr (E. Ozensoy).

0920-5861/$ – see front matter © 2014 Elsevier B.V. All rights reserved.
http://dx.doi.org/10.1016/j.cattod.2013.12.037

tolerance, material preparation, NO_x storage capacity and thermal stability aspects. Takahashi et al. [20] investigated the influence of the relative abundance of TiO_2 and ZrO_2 components and found that the NSR system that was comprised of 70 wt% ZrO_2 and 30 wt% TiO_2 exhibited the best sulfur tolerance. Imagawa et al. [21,22] reported a detailed characterization study related to the $Al_2O_3/ZrO_2/TiO_2$ ternary oxide system emphasizing the impact of Al_2O_3 incorporation into the ZrO_2/TiO_2 mixed oxide where it was indicated that nano-composite $Al_2O_3/ZrO_2/TiO_2$ had a higher NO_x storage capacity and a higher thermal resistance as compared to the physically mixed Al_2O_3 and ZrO_2/TiO_2.

Thus, in the current study, we aimed to provide a mechanistic view into the NO_x storage and reduction pathways of binary and ternary mixed oxides by monitoring the nitrate reduction via H_2 at the molecular level by means of in situ FTIR and TPD.

2. Experimental

2.1. Material preparation

ZrO_2/TiO_2 binary and $Al_2O_3/ZrO_2/TiO_2$ ternary oxides were synthesized using the conventional sol–gel method. For the synthesis of the binary oxides, zirconium propoxide (Sigma Aldrich, ACS Reagent, 70 wt% in 1-propanol) and titanium(IV) isopropoxide (Sigma Aldrich, ACS Reagent, 97%) precursors were initially dissolved in 100 ml of 2-propanol (Sigma Aldrich, ACS Reagent >99.5%) and stirred for 40 min under ambient conditions. This step was followed by the drop-wise addition of 3 mL of 0.5 M nitric acid solution (Sigma Aldrich, ACS Reagent, 65%) in order to obtain a gel. Similarly, the synthesis of the ternary oxide was carried out by mixing zirconium isopropoxide, titanium isopropoxide and aluminum sec-butoxide (Sigma Aldrich, ACS Reagent, 97%) followed by the addition of 100 mL of 2-propanol. Next, the slurry was stirred for 60 min under ambient conditions and gel formation was achieved by drop-wise addition of 9 mL of 0.5 M nitric acid solution. In the binary oxide, the composition ratio of ZrO_2:TiO_2 was 70:30 by mass. This specific ratio has been reported as the optimum candidate for the highest NO_x removal ability and the highest tolerance against sulfur-poisoning [20]. Finally, the materials were dried under ambient conditions for 48 h followed by calcination in air within 323–1173 K. Relative composition of the ternary oxide system (i.e. $Al_2O_3/ZrO_2/TiO_2$) by mass was 50:35:15 [20]. 1 wt% platinum-incorporated binary and ternary oxide materials were synthesized by incipient wetness impregnation method using a solution of $Pt(NH_3)_2(NO_2)_2$ (Aldrich, diamminedinitritoplatinum(II), 3.4 wt% solution in dilute NH_3(aq)). Prior to the Pt addition, ZrO_2/TiO_2 and $Al_2O_3/ZrO_2/TiO_2$ were initially calcined in air at 773 K for 150 min in order to remove the organic functionalities in the precursors. Finally, each material was subsequently calcined in air at 973 K for nitrite/nitrate content elimination and structural stabilization. In the current text, synthesized ZrO_2/TiO_2, $Al_2O_3/ZrO_2/TiO_2$, $Pt/ZrO_2/TiO_2$, $Pt/Al_2O_3/ZrO_2/TiO_2$ samples will be abbreviated as ZT, AZT, Pt/ZT and Pt/AZT, respectively.

2.2. Instrumentation

Detailed description of the instrumentation used in the currently presented experiments involving X-ray diffraction (XRD), Raman spectroscopy, BET surface area analysis, temperature programmed desorption (TPD) and in situ FTIR can be found elsewhere [8]. Briefly, in situ FTIR spectroscopic measurements were performed in transmission mode using a Bruker Tensor 27 FTIR spectrometer which was modified to house a batch-type spectroscopic reactor coupled to a quadrupole mass spectrometer (QMS, Stanford Research Systems, RGA 200) for TPD measurements.

Each synthesized material was exposed to NO_2(g) which was prepared by mixing NO(g) (Air Products, 99.9%) and excess O_2(g) (Linde GmbH, Germany, 99.999%). Freeze–thaw-pump cycles were applied for the removal of contaminations and unreacted gases in the NO_2(g). The material surfaces were initially flushed with 1.0 Torr of NO_2(g) for 5 min and subsequently annealed to 973 K with a 12 K/min heating rate under vacuum. Then, for the FTIR analysis, material surfaces were exposed to NO_2(g) at 323 K in a stepwise fashion from low to higher pressures where each exposure takes 1 min. Finally, surface saturation was achieved by the introduction of 5.0 Torr NO_2(g) over the samples for 10 min at 323 K followed by evacuation to a pressure lower than 10^{-2} Torr.

Nitrate reduction experiments for the Pt-free materials were carried out by exposing the NO_2(g)-saturated material surface to 15.0 Torr of H_2(g) (Linde GmbH, Germany, >99.9%) at 323 K, followed by gradual heating at a constant rate of 12 K/min until the desired temperature. For the Pt-containing materials, 15.0 Torr of H_2(g) was introduced over the NO_2-saturated material at 323 K and the time-dependent FTIR spectra were acquired for 2 h. After 2 h of reduction at 323 K, sample was heated up to 473 K in the presence of H_2(g) for the complete reduction and removal of adsorbed NO_x. All of the FTIR spectra given in this study were obtained at 323 K.

In TPD experiments, each sample was saturated by NO_2(g) as described above. Subsequently, saturated materials were heated up to 973 K with a linear heating rate of 12 K/min in vacuum. FTIR spectra of the corresponding surfaces were also recorded before and after the TPD experiments.

3. Results and discussion

3.1. Structural characterization of the synthesized materials

Fig. 1 illustrates ex situ XRD analysis for the ZT and AZT materials recorded after calcination at various temperatures in the range of 323–1173 K. As shown in Fig. 1a, the amorphous structure of ZT binary oxide persists up to 773 K followed by the formation of crystalline phases above 773 K, namely tetragonal ZrO_2 and $ZrTiO_4$. The structural evolution of AZT is also shown by XRD in Fig. 1b where the ternary oxide system behaves quite differently compared to the binary oxide. AZT preserved its amorphous nature up to 973 K without revealing any well-resolved diffraction signals. Along these lines, AZT showed only poorly discernible diffraction signals at $2\theta = 30.48^\circ$, 50.50°, 60.91° corresponding to tetragonal ZrO_2 (JCPDS 80-2155) at 1173 K. Apparently, the addition of an alumina component to the ZT system elevates the ordering/crystallization temperatures and suppresses the formation of $ZrTiO_4$ (JCPDS 34-415). It is worth mentioning that XRD analysis was also performed for the Pt/ZT and Pt/AZT materials (Supporting Information Fig. 1), where it was observed that Pt addition did not lead to a major crystallographic change over the ZT and AZT systems besides the presence of diffraction signals associated with metallic Pt particles.

The temperature-dependent Raman spectra of ZT and AZT are illustrated in Fig. 2. $ZrTiO_4$, one of the main crystalline phases detected for ZT samples in XRD, has an orthorhombic symmetry with a *Pbcn* space group and a *mmm* point group. This phase has 33 optically active modes, 18 of which are Raman active [23,24]. However, in the Raman data corresponding to the ZT sample presented in Fig. 2a, only six of these vibrational features at 135, 259, 320, 391, 565 and 778 cm^{-1} are discernible. This can be associated with the band broadening and signal overlap due to the random distribution of Zr^{4+} and Ti^{4+} ions in the crystal lattice [23,24]. Raman shifts at 467 and 622 cm^{-1} in Fig. 2a corresponding to the ZT sample are most likely associated with the tetragonal ZrO_2 phase, while the

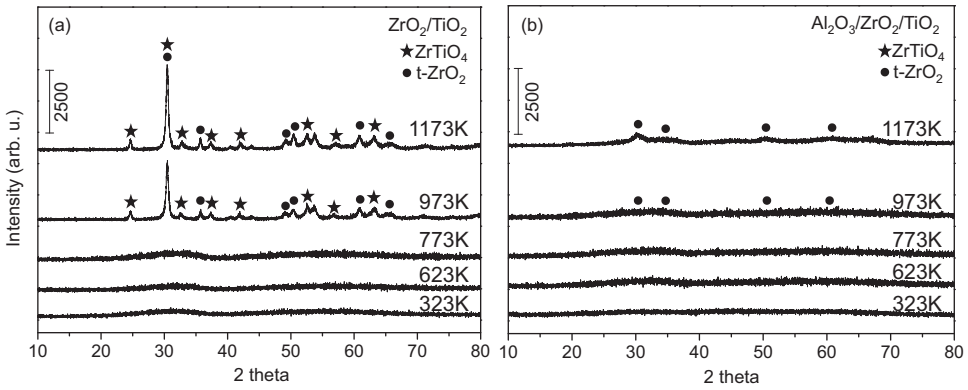

Fig. 1. XRD patterns corresponding to (a) ZrO_2/TiO_2 and (b) $Al_2O_3/ZrO_2/TiO_2$ materials upon calcination at temperatures within of 323–1173 K.

feature at 391 cm^{-1} can be attributed to the presence zirconium titanate phase [25,26].

As compared to the ZT binary oxide, Raman spectra corresponding to the AZT ternary oxide sample (Fig. 2b) revealed much weaker signals due to the poor crystallinity and the lack of atomic order in the latter sample. In Fig. 2b, three weak Raman features located at 320, 465 and 625 cm^{-1} are visible which can be attributed to the tetragonal zirconia phase. This reveals that besides the tetragonal ZrO_2 phase, XRD and Raman data do not provide any clear indications for the presence of additional ordered phases in the AZT system, such as $ZrTiO_4$. These observations are in line with studies reported by Escobar et al. [27] who suggested that in the ZT binary system ZrO_2 can provide Zr^{4+} ions which may diffuse into the TiO_2 lattice in the absence of aluminum oxide, forming $ZrTiO_4$. However, in the AZT ternary system, XRD and Raman data given in Figs. 1 and 2 suggest that Al_2O_3 acts as a diffusion barrier preventing diffusion of Zr^{4+} ions in to the TiO_2 lattice, preventing the ordering of the crystal lattice and the formation $ZrTiO_4$.

Fig. 3 presents the BET specific surface area (SSA) values for the synthesized materials which were calcined at 773, 973 and 1173 K. Fig. 3 indicates that the AZT ternary oxide system has a much higher surface area compared to the ZT binary oxide system for all calcination temperatures. While the ternary oxide system has almost two-fold greater surface area at 773 K, this gap was observed to extend up to a ten-fold difference at 973 K. These results are in very good agreement with the current XRD and Raman results suggesting a more disordered structure for the AZT system. Crystallization of the ZT binary oxide leads to relatively ordered and larger particles at 973 K, while the ternary system preserves its rather amorphous structure and small particle size even at 1173 K. It is worth mentioning that on account of the different Ti and Zr precursors used in the current work, synthesized ternary oxide material (i.e. $Al_2O_3/ZrO_2/TiO_2$) has a higher surface area (i.e. SSA 264 m^2/g) compared to the nano-composite ternary oxide material with a SSA ~200 m^2/g which was reported in a recent study [20]. BET SSA analysis was also performed for Pt-containing samples which were prepared as described in the experimental section. These measurements showed that although Pt addition and subsequent calcination at 973 K did not have a significant influence on the SSA values of the ZT system (26 m^2/g versus 37 m^2/g for ZT and Pt/ZT, respectively), SSA values of the AZT system significantly decreased in the presence of Pt (264 m^2/g versus 191 m^2/g for AZT

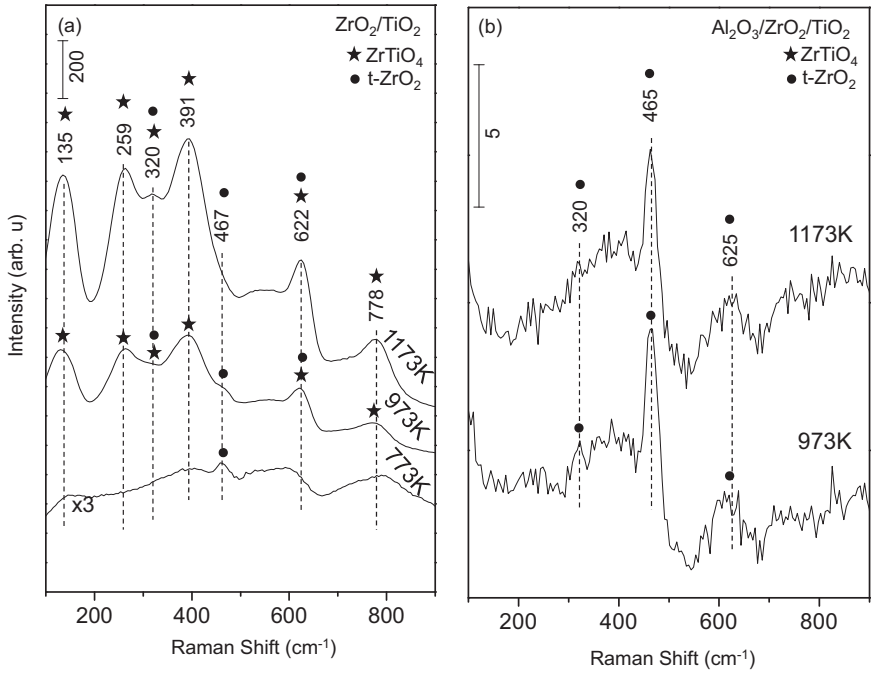

Fig. 2. Ex situ Raman spectra corresponding to (a) ZrO_2/TiO_2 and (b) $Al_2O_3/ZrO_2/TiO_2$ materials upon calcination at temperatures within 773–1173 K.

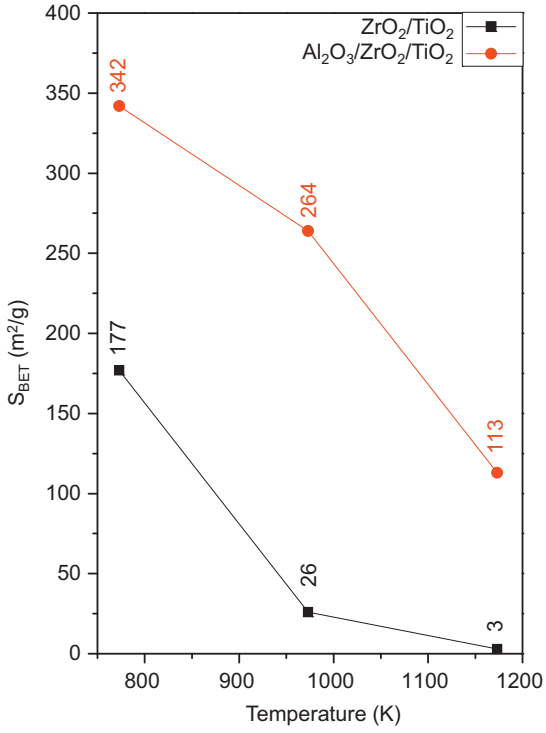

Fig. 3. BET specific surface area values for (a) ZrO_2/TiO_2 (black) and $Al_2O_3/ZrO_2/TiO_2$ (red) after calcination at temperatures within 773–1173 K.

and Pt/AZT, respectively). Along these lines, it can be argued that Pt sites facilitate the oxidation of the AZT matrix during the calcination carried out at 979 K, which results in a more ordered ternary oxide system with larger ZrO_2 and TiO_2 crystallites. However these crystallites still seem to be small enough to be elusive in XRD (Supporting Information Fig. 1). Further evidence for this argument will be provided along with the discussion of the TPD results for the AZT and Pt/AZT samples given in the next section.

3.2. $NO_2(g)$ adsorption and desorption on ZrO_2/TiO_2 and $Al_2O_3/ZrO_2/TiO_2$

Fig. 4 represents the FTIR spectra corresponding to $NO_2(g)$ adsorption on both of the binary and ternary oxide materials (already calcined at 973 K) at 323 K for increasing exposures. Five particular vibrational features were detected for ZT which were located at 1644, 1578, 1550, 1280 and 1209 cm^{-1} as illustrated in Fig. 4a. The spectral region between 1700 and 1200 cm^{-1} is characteristic for the nitrate and nitrite species coordinated on TiO_2 and ZrO_2 [28–30]. The observed frequencies at 1644 and 1209 cm^{-1} can be attributed to bridging nitrates, while the features at 1578, 1550 and 1280 cm^{-1} can be assigned to bidentate nitrates [8,31]. Similar absorption features also appeared for the AZT ternary oxide system as shown in Fig. 4b. However, the position of bridging nitrates (1639 and 1244 cm^{-1}) on the AZT ternary oxide is different when compared to the ZT binary oxide system. Probably, the most prominent aspect of Fig. 4 is the dissimilarity in the relative FTIR intensities of AZT and ZT systems. It is clear that the NO_x adsorption on the AZT ternary oxide is significantly higher than that of the ZT binary oxide due to a ten-fold higher specific surface area and the significantly greater IR absorption intensity upon NO_x adsorption of the former surface at 973 K.

More quantitative insight into the total NO_x adsorption capability and thermal stability of adsorbed nitrate species can be obtained by combining FTIR and TPD results. TPD profiles related to the ZT and AZT systems obtained after $NO_2(g)$ saturation (5.0 Torr for 10 min) at 323 K are presented in Fig. 5a and b, respectively. Comparison of the TPD line shapes for ZT and AZT systems immediately reveals the dissimilar NO_x desorption characteristics on each material. While most of the NO_x desorption is completed below 800 K for the ZT sample, this is not true for AZT where even at 1000 K, NO_x desorption is still incomplete. NO ($m/z = 30$) desorption signal for the ZT sample (Fig. 5a) shows two major features at of 640 and 750 K related to the nitrate decomposition. In the first desorption state of 640 K, nitrate decomposition takes place by simultaneous evolution of NO, O_2, N_2O and NO_2 corresponding to m/z signals at 30, 32, 44 and 46, respectively. On the other hand, the high temperature nitrate desorption state (750 K) of the ZT system reveals primarily NO and N_2O with a lesser contribution from O_2 and NO_2.

NO ($m/z = 30$) desorption signal for the AZT system in Fig. 5b indicates that within the temperature window of the current TPD experiments (i.e. 323–973 K), NO_x desorption was not completed. This trend indicates that the relative thermal stability of the stored NO_x species (i.e. nitrates) on the AZT surface is much higher than that of the ZT surface. This can at least be partially attributed to the existence of a large concentration of surface defects and coordinatively unsaturated adsorption sites which are present on the disordered/poorly crystalline AZT surface revealing a higher SSA. Furthermore, comparison of the TPD signal intensities for ZT and AZT samples reveals that the NO_x adsorption of the AZT ternary oxide is far greater than that of the ZT binary oxide (i.e. the total integrated NO_x-uptake related desorption signal comprised of $NO + NO_2 + N_2 + N_2O$ desorption channels is %143 greater for AZT. Reader is referred to the Supporting Information section for the details of the TPD integrated signal analysis). In addition, Fig. 5b also suggests that the nitrate decomposition on the AZT

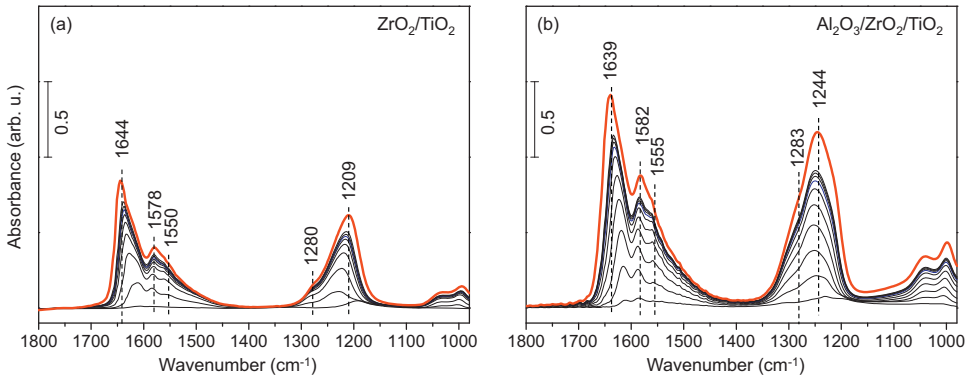

Fig. 4. FTIR spectra corresponding to the stepwise $NO_2(g)$ adsorption at 323 K on (a) ZrO_2/TiO_2 and (b) $Al_2O_3/ZrO_2/TiO_2$ surfaces. The bold (red) spectrum in each panel corresponds to the NO_x-saturated (5.0 Torr $NO_2(g)$ for 10 min at 323 K) surface. (For interpretation of the references to color in this figure legend, the reader is referred to the web version of the article.)

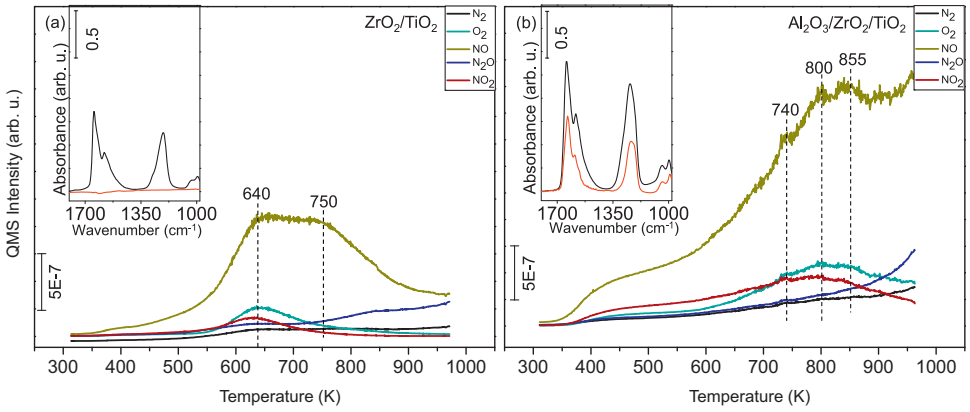

Fig. 5. TPD profiles obtained from (a) ZrO_2/TiO_2 and (b) $Al_2O_3/ZrO_2/TiO_2$ samples after saturation with 5 Torr NO_2(g) at 323 K for 10 min. The inset in each panel presents the FTIR spectra of the surfaces before (black) and after (red) TPD analysis. (For interpretation of the references to color in this figure legend, the reader is referred to the web version of the article.)

surface occurs via evolution of mostly NO, O_2 and NO_2 with a relatively insignificant contribution from other desorption channels. These TPD results are in perfect agreement with the corresponding in situ FTIR data presented as insets in Fig. 5a and b. In these insets, black curves correspond to NO_2-saturated surfaces before the TPD experiments, while the red curves correspond to the ZT and AZT surfaces after the TPD analysis (i.e. after annealing under vacuum at 973 K). FTIR data clearly show that while complete nitrate elimination was achieved on ZrO_2/TiO_2 after the TPD experiment, a significant amount of nitrate species observed to be remaining on the AZT surface after the TPD run.

The effect of Pt incorporation on NO_x adsorption geometry and storage capacity was also investigated via in situ FTIR spectroscopy and TPD. FTIR studies involving NO_x adsorption experiments on $Pt/ZrO_2/TiO_2$ and $Pt/Al_2O_3/ZrO_2/TiO_2$ (Supporting Information Fig. 2) lead us to conclude that the presence of Pt has no significant influence on the NO_x adsorption geometries. Fig. 6 shows the TPD profiles obtained after NO_2 saturation on $Pt/ZrO_2/TiO_2$ and $Pt/Al_2O_3/ZrO_2/TiO_2$ at 323 K. In Fig. 6a, two NO desorption states that belong to $Pt/ZrO_2/TiO_2$ at 630 and 755 K are visible, as in the case of ZrO_2/TiO_2 (Fig. 5a). However, the high temperature desorption state located at 755 K is significantly suppressed in the presence of platinum. This implies that on the $Pt/ZrO_2/TiO_2$ surface, Pt sites facilitate the decomposition of strongly bound nitrate species, shifting their decomposition temperatures to lower values. Furthermore, comparison of the TPD data given in Figs. 5a and 6a suggests that Pt addition significantly increases the relative desorption of N_2 and N_2O for the $Pt/ZrO_2/TiO_2$. This can possibly be due to the Pt-catalyzed direct partial/total reduction of the adsorbed nitrates on the $Pt/ZrO_2/TiO_2$ sample into N_2 and N_2O, particularly at 755 K. Lack of a significant O_2 desorption signal at 755 K, indicates that the oxidizing species such as atomic oxygen or diatomic oxygen generated during the partial/total reduction of nitrates are possibly captured by the $Pt/ZrO_2/TiO_2$ system where they may oxidize Pt sites and/or titrate oxygen defects in the tetragonal ZrO_2 or $ZrTiO_4$ phases. It is also worth mentioning that comparison of the integrated TPD desorption signals for the ZrO_2/TiO_2 (Fig. 5a) and $Pt/ZrO_2/TiO_2$ (Fig. 6a) indicates that Pt addition to the ZT system significantly boosts the NO_x adsorption. Numerically, Pt addition to the ZT system increases the integrated NO desorption signal by about 32% and increases the total integrated NO_x-uptake related desorption signal associated with $NO + NO_2 + N_2 + N_2O$ by 101% (see Supporting Information section for details). Note that these numbers do not correspond to NO_x storage capacity (NSC) values and used merely for the semi-quantitative comparison of the relative NO_x uptakes of the investigated surfaces.

Investigation of the TPD data given in Fig. 6b indicates that the influence of the Pt sites on the nitrate decomposition is much more prominent for the AZT system. Firstly, Pt incorporation seems to promote more facile thermal nitrate decomposition on the $Al_2O_3/ZrO_2/TiO_2$ ternary oxide system, where the NO ($m/z = 30$) desorption maxima are significantly shifted to lower temperatures. More interestingly, NO desorption maxima for the Pt/AZT system (640 and 730 K, Fig. 6b) are almost identical to that of ZT (640 and 750 K, Fig. 5a) and Pt/ZT (630 and 730 K, Fig. 6a) and quite unlike AZT (740, 800, 855 K, Fig. 5b). Combining this observation with the SSA values obtained for these systems discussed earlier implies that although AZT system is comprised of a quite disordered and a rather defective ternary oxide system, Pt/AZT system consists of more ordered finely dispersed small particles of ZrO_2, TiO_2, $ZrTiO_4$ and Al_2O_3. These particles are possibly formed during the calcination step, where Pt sites oxidize the AZT surface, increasing the crystallographic order of the surface to a certain extent, which is elusive to detect via bulk characterization techniques such as XRD (Supporting Information Fig. 1). Presence of Al_2O_3 domains on the Pt/AZT surface is also supported by the existence of the NO desorption shoulder at 400–450 K in Fig. 6b (concomitant to a NO_2 signal which also appears at the same temperature window) which is a characteristic feature of NO_2 TPD from γ-Al_2O_3 [32] Although this 400 K NO_x desorption feature is absent for ZT and Pt/ZT samples (Figs. 5a and 6), it is visible (though with a much smaller intensity) for the AZT sample, suggesting that the alumina domains on the AZT sample are much less fully oxidized/ordered. Since the NO_x desorption/decomposition was incomplete for the AZT sample within the thermal window of the TPD analysis, it is difficult to make a quantitative comparison for the NO_x uptake of AZT versus Pt/AZT systems. However analysis of the integrated TPD signals associated with AZT (Fig. 5b) and Pt/AZT (Fig. 6b) samples shows that Pt addition to the AZT system increases the integrated NO desorption signal more than 288% and increases the total integrated NO_x-uptake related desorption signal associated with $NO + NO_2 + N_2 + N_2O$ by more than 50%. It can also be noted that although the 640 K NO_x desorption from the Pt/AZT surface occurs in the form of NO, O_2 and NO_2; NO_x desorption at 730 K takes place with the evolution of NO and O_2 only.

On the other hand, relative NO_x adsorption amounts should be also assessed considering the relative specific surface area value for each material. Our calculations indicate that Pt incorporation to the ZT binary oxide system increases the total integrated NO_x-uptake/m^2 by 41%. Moreover, in the AZT ternary oxide system, Pt plays a much more effective role in increasing the total integrated NO_x uptake/m^2 by 109%.

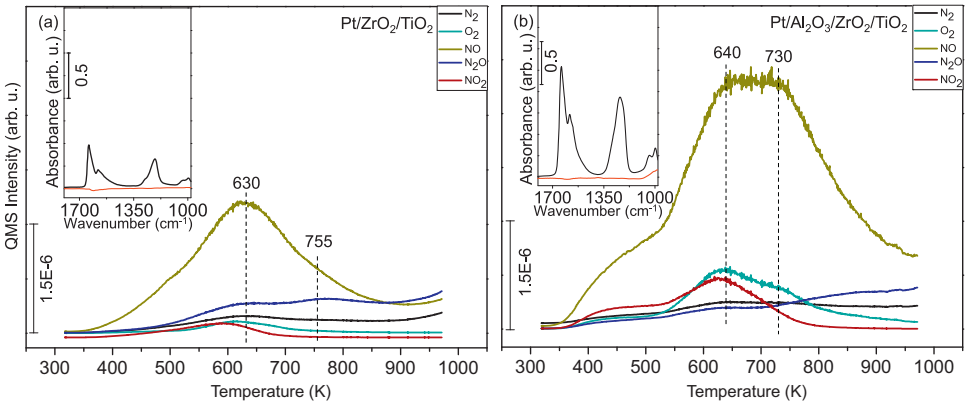

Fig. 6. TPD profiles obtained from (a) $Pt/ZrO_2/TiO_2$ and (b) $Pt/Al_2O_3/ZrO_2/TiO_2$ samples after saturation with 5 Torr NO_2(g) at 323 K for 10 min. The inset in each panel shows the FTIR spectra of the surfaces before (black) and after (red) TPD analysis. (For interpretation of the references to color in this figure legend, the reader is referred to the web version of the article.)

Trends observed for the TPD data given in Fig. 6 are in very good agreement with the corresponding FTIR spectra obtained before and after the TPD runs which are given as insets of Fig. 6. Particularly, the inset of Fig. 6b shows how Pt plays a significant role in the nitrate decomposition performance of the AZT ternary oxide system. As shown in the inset of Fig. 6b, Pt/AZT surface was completely free of adsorbed NO_x species after the TPD run (i.e. after annealing at 973 K) while this was not the case for the Pt-free AZT counterpart (inset of Fig. 5b).

Current results discussed above allows us to consider the AZT system as a promising candidate material for low-temperature NSR applications. Compared to the conventional Pt/20 wt%BaO/Al_2O_3 system, Pt/AZT material calcined at 973 K has a specific surface area of 191 m^2/g, while conventional Pt/20 wt%BaO/Al_2O_3 has a SSA of 125 m^2/g. On the other hand, although Pt/20 wt%BaO/Al_2O_3 has a lower surface area, it has 19% greater integrated total NO_x desorption signal than Pt/AZT70 obtained via identical adsorption experiments (data not shown). Influence of the BaO domains on the NO_x adsorption and release properties of ZT and AZT systems is an interesting aspect which will be discussed in detail in a forthcoming report [33].

3.3. NO_x reduction on binary and ternary oxide systems via H_2(g)

As well as the NO_x storage characteristics of ZT and AZT materials, their NO_x reduction/regeneration performances under reducing conditions should also be taken into consideration for the sake of NSR applications. Reduction resistance of nitrate species on Pt-free ZT and AZT materials was investigated via FTIR spectroscopy in the presence of an external reducing agent (i.e. H_2(g)), as illustrated in Fig. 7a and b, respectively. Prior to nitrate reduction, the material surfaces were saturated with 5.0 Torr NO_2(g) for 10 min at 323 K. After the saturation of the surface with NO_2(g), 15.0 Torr of H_2(g) was introduced over the sample surface. Temperature-dependent FTIR spectra were obtained after annealing the NO_2-saturated surfaces at 373, 473, 573, 623, 673, 723 K in the presence of H_2(g). Adsorbed nitrates on ZT (Fig. 7a) fully survived under reducing conditions up to 473 K with only minor IR intensity changes. However, the IR signal intensities started to decrease at 573 K, where significant amounts of nitrates were lost from the surface. It is also apparent in Fig. 7a that bidentate nitrates (1580 cm^{-1}) are relatively more stable than bridging nitrates (1649 cm^{-1}) under reducing conditions on the binary oxide system. Finally, complete removal of nitrates on the ZT surface under H_2(g) environment was achieved at 623 K (corresponding to the red spectrum in Fig. 7a); a temperature that is compatible with the thermal window of realistic exhaust emission control systems.

Similar experiments were also performed on the AZT ternary oxide system (Fig. 7b). As discussed above, adsorbed nitrates on AZT reveal a very high thermal stability in a H_2-free environment. Even under reducing conditions, nitrates on AZT surface were found to be quite stable even at 573 K (Fig. 7b). FTIR analysis clearly indicates that under reducing conditions, all of the nitrate species on AZT can be completely reduced at 723 K.

Our preliminary experiments (data not shown) related to elevated-temperature nitrate reduction on Pt-containing

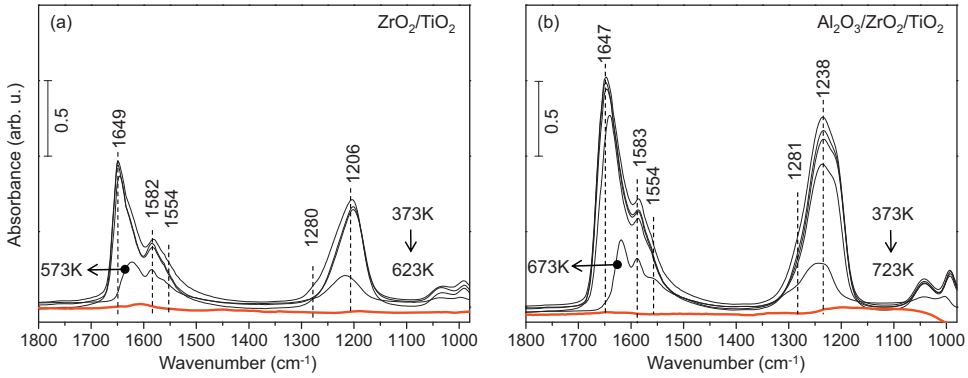

Fig. 7. FTIR spectra corresponding to the temperature-dependent nitrate reduction via 15.0 Torr of H_2(g) on (a) ZrO_2/TiO_2 and (b) $Al_2O_3/ZrO_2/TiO_2$ surfaces. The topmost spectrum in each panel corresponds to the NO_x-saturated (5.0 Torr NO_2(g) for 10 min at 323 K) surface. The series of black spectra in each panel were collected at different temperatures within 323–723 K. The bottommost (red) spectrum in each panel corresponds to the highest reduction temperature exploited (i.e. 623 K for ZT and 723 K for AZT). (For interpretation of the references to color in this figure legend, the reader is referred to the web version of the article.)

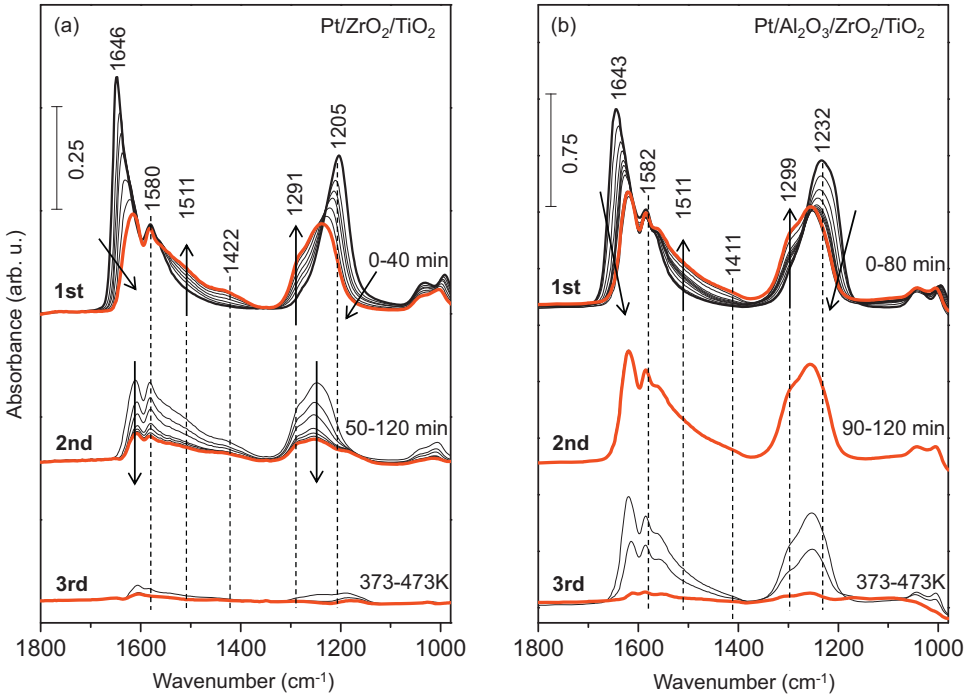

Fig. 8. FTIR spectra corresponding to the time-dependent nitrate reduction via 15.0 Torr of H_2(g) on (a) $Pt/ZrO_2/TiO_2$ and (b) $Pt/Al_2O_3/ZrO_2/TiO_2$ surfaces. The topmost spectrum in each panel corresponds to the NO_x-saturated (5.0 Torr NO_2(g) for 10 min at 323 K) surface. The series of spectra in the "1st" and "2nd" intervals were collected as a function of time during the initial 120 min of reduction at 323 K. "1st" interval corresponds to the 0–40 min or 0–80 min of the initial reduction periods for $Pt/ZrO_2/TiO_2$ and $Pt/Al_2O_3/ZrO_2/TiO_2$, respectively; while the "2nd" interval corresponds to the remaining time evolution until 120 min of reduction. FTIR spectra in the "3rd" interval were collected after the initial 120 min reduction at 323 K by increasing to temperature to 373, 423 and 473 K in the presence of H_2(g).

materials (i.e. Pt/ZT and Pt/AZT) revealed extremely fast reaction even at relatively lower temperatures, rendering mechanistic comparison of these two systems rather difficult. Therefore, time-dependent experiments were carried out with slower kinetics at low temperatures (i.e. 323 K) in order to monitor and elucidate the temporal changes in the surface functional groups on material surfaces upon reduction by H_2(g). Fig. 8 illustrates the corresponding FTIR spectra for Pt/ZT and Pt/AZT recorded as a function of time after NO_x saturated (5.0 Torr NO_2 for 10 min) material surface was exposed to 15.0 Torr of H_2(g). For the sake of clarity, each panel in Fig. 8 is divided into three time intervals. The first interval of the data set in Fig. 8a is related to the initial reduction period of 40 min at 323 K. In the first period, while the intensities characteristic for bridging nitrates (1646 and 1205 cm^{-1}) diminish, other vibrational features at 1511 and 1291 cm^{-1} corresponding to monodentate nitrate species simultaneously start to emerge [31]. Another growing feature in this period observed at 1422 cm^{-1} (together with 1291 cm^{-1}) can be assigned to nitrites [34]. For the second time interval between 50 and 120 min, initially formed monodentate nitrates and nitrites concurrently attenuate upon interaction with H_2(g) together with all other nitrate species such as bridging and bidentate nitrates. Since the NO_x reduction on Pt/ZT has mostly ceased after 120 min (Fig. 8a), in the third stage, the material was annealed to higher temperatures in H_2(g) in order to eliminate any remaining NO_x species on the surface. The spectra in the third interval corresponding to the reduction of nitrites and nitrates on the material surface were collected at 373, 423 and 473 K. These results allow us to obtain a better insight regarding the nitrate reduction mechanism on the Pt/ZT surface under H_2(g) atmosphere which initially takes place via transformation of bridging nitrates into monodentate nitrates and nitrites followed by the complete removal of all NO_x species around 473 K.

An identical set of experiments was also performed for the Pt/AZT surface (Fig. 8b). As the reducing agent H_2(g) is introduced over the NO_x-saturated surface, the intensities of the vibrational features at 1643 and 1232 cm^{-1} (bridging nitrates) attenuate together with increase in the intensities of 1511 and 1299 cm^{-1} (monodentate nitrates) as well as 1411 cm^{-1} (nitrites). A noteworthy difference between the binary and ternary systems is that while all nitrate-related stretching signals diminish in the second time interval at 323 K on Pt/ZT (Fig. 8a), no spectral changes were observed in the second time interval (90–120 min) of the Pt/AZT system (Fig. 8b). These observations are in harmony with previous TPD and FTIR results indicating that adsorbed NO_x species typically possess a higher stability on the AZT surface than ZT. Similar to the ZT system, almost all of the adsorbed NO_x species can be eliminated from the Pt/AZT surface in the presence of H_2(g) at 473 K. It is worth mentioning that comparison of the NO_x reduction capabilities of the Pt/AZT system with conventional NSR systems that we have investigated in the past such as Pt/20 wt%BaO/Al_2O_3 and Pt/20 wt%BaO/20 wt%CeO_2/Al_2O_3 [8], reveals that reduction of adsorbed NO_x species with H_2(g) at 473 K occurs in a more facile manner on the Pt/AZT surface.

Fig. 9 illustrates the region of the in situ FTIR spectra associated with the —OH and —NH_x stretching regions of the Pt/ZT system, which were acquired during the time-dependent reduction experiments described above along with the data presented in Fig. 8. Fig. 9a and b shows the evolution of the in situ FTIR spectra for the first (0–40 min) and the second (50–120 min) time intervals of the nitrate reduction via H_2(g), respectively. Upon NO_2(g) introduction to the Pt/ZT surface (5.0 Torr NO_2(g) for 10 min), negative features at 3722 and 3678 cm^{-1} were observed (Fig. 9a). While the former feature has been assigned to linear (type-I) —OH species, the latter one is characteristics for three-fold (type-III) hydroxyls [35–42] which disappear from the surface upon interaction/coordination with adsorbed nitrates and nitrites. Another broad and highly convoluted feature centered at 3512 cm^{-1} can be attributed to H-bonded surface hydroxyl species [38,39]. In Fig. 9a, the interaction of H_2

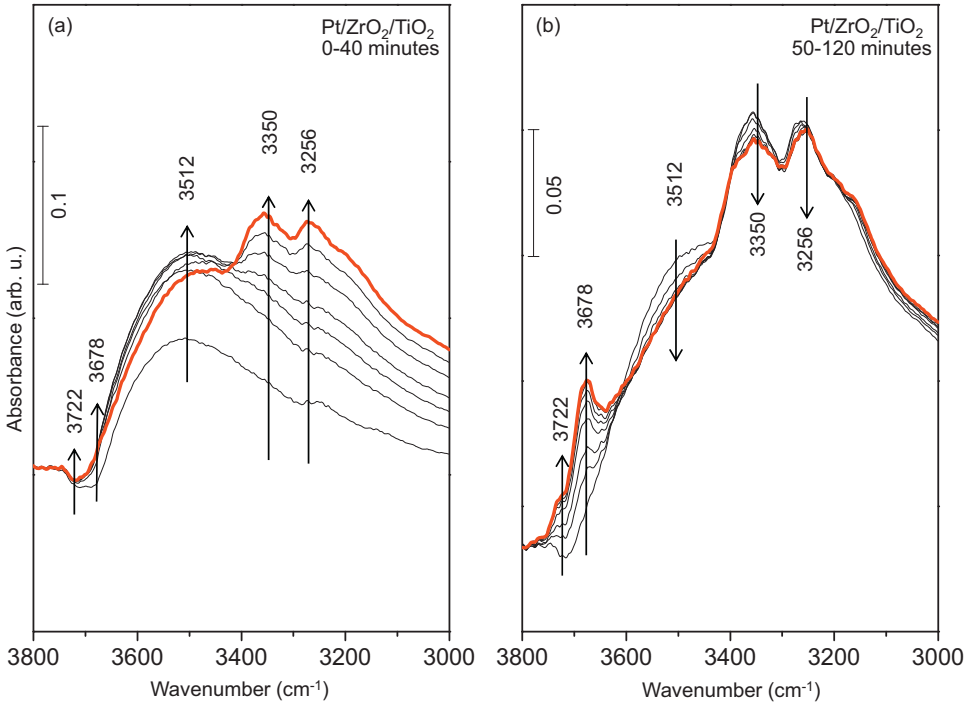

Fig. 9. OH/—NH stretching region of the in situ FTIR spectra corresponding to NO_2 adsorption and saturation (5.0 Torr NO_2(g) for 10 min at 323 K) followed by subsequent reduction with 15.0 Torr of H_2(g) on $Pt/ZrO_2/TiO_2$ at 323 K during (a) 0–40 min of reduction and (b) 50–120 min of reduction. Bold (red) spectrum in each panel corresponds to the last spectrum obtained at the end of the given time interval. (For interpretation of the references to color in this figure legend, the reader is referred to the web version of the article.)

with nitrate species on the $Pt/ZrO_2/TiO_2$ surface in the first time interval can be followed by the gradually emerging vibrational frequencies at 3350 and 3256 cm^{-1} related to —NH stretchings and the growing feature at 3512 cm^{-1} related to H-bonded surface hydroxyls [43,44]. Therefore in the first time interval (0–40 min), it is apparent that the nitrate reduction mechanism involves conversion of bridging nitrates into monodentate nitrates and nitrites together with the formation of H-bonded surface hydroxyl groups

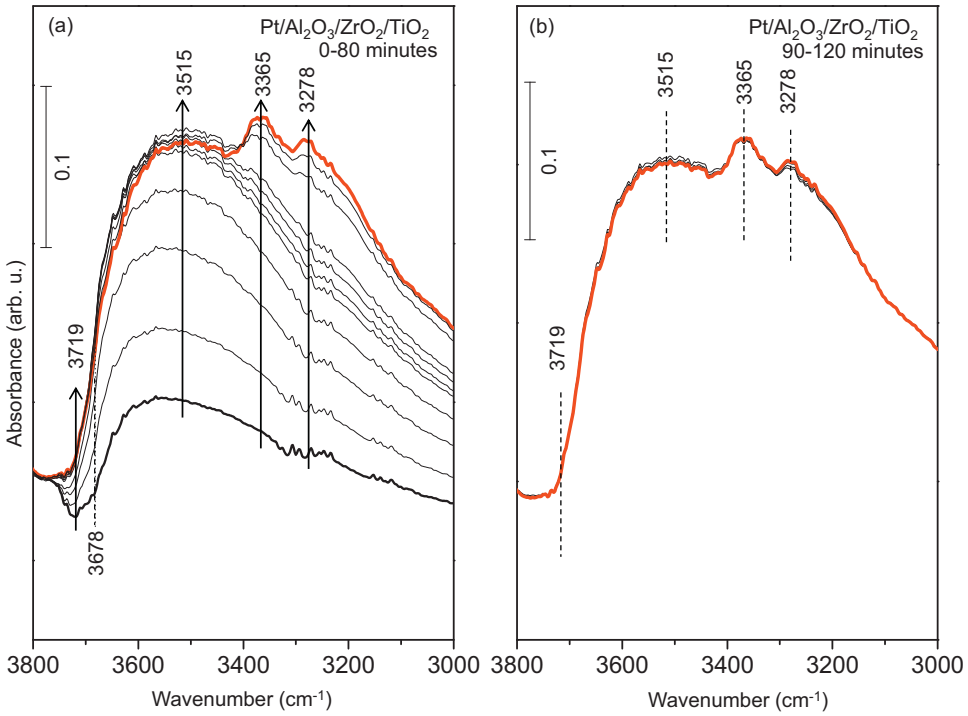

Fig. 10. OH/–NH stretching region of the in situ FTIR spectra corresponding to NO_2 adsorption and saturation (5.0 Torr NO_2(g) for 10 min at 323 K) followed by subsequent reduction with 15.0 Torr of H_2(g) on $Pt/Al_2O_3/ZrO_2/TiO_2$ at 323 K during (a) 0–80 min of reduction and (b) 90–120 min of reduction. Bold (red) spectrum in each panel corresponds to the last spectrum obtained at the end of the given time interval. (For interpretation of the references to color in this figure legend, the reader is referred to the web version of the article.)

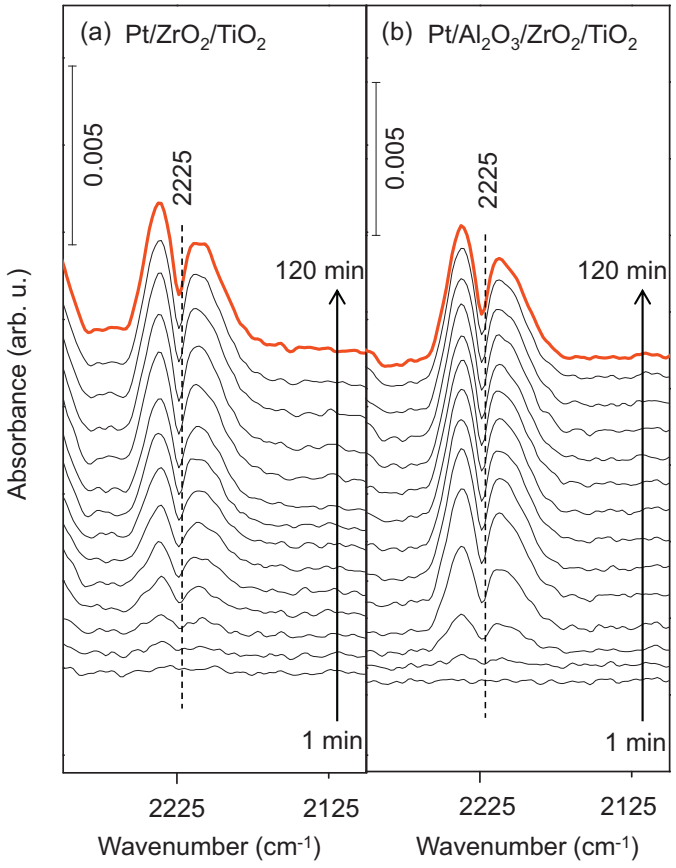

Fig. 11. Time-dependent in situ gas phase FTIR spectra corresponding to nitrate reduction via 15.0 Torr of H_2(g) on (a) $Pt/ZrO_2/TiO_2$ and (b) $Pt/Al_2O_3/ZrO_2/TiO_2$ at 323 K for 120 min. Red spectrum in each panel corresponds to the last spectrum obtained at the end of the given time interval. (For interpretation of the references to color in this figure legend, the reader is referred to the web version of the article.)

and —NH functionalities which might be associated with $—NH_2$, $—NH_3$, $—OH\cdots NH_x$ or $—OH\cdots NO_x$ species [8,43,44].

In situ FTIR data presented in Fig. 9b shows additional significant spectral changes in the course of the second time interval (50–120 min) of reduction, during which a large portion of the nitrate groups were reduced by H_2. During this period, while the isolated terminal and bridging —OH species (initially present negative features at 3722 and 3678 cm^{-1}) were regenerated, the feature at 3512 cm^{-1} related to H-bonded surface hydroxyl species diminished. In other words, as the nitrates were eliminated from the surface, $—OH\cdots NH_x$ or $—OH\cdots NO_x$ interactions seized to exist and some of the surface —OH functionalities were converted into isolated hydroxyls.

Fig. 10 illustrates the same set of experiments performed on the Pt/AZT system. Similar to Pt/ZT, in the first time interval of H_2(g) interaction (0–80 min) with the NO_x-saturated surface reveals a gradual increase of the vibrational intensities at 3515 cm^{-1} related to H-bonded hydroxyl species and newly formed features at 3365 and 3278 cm^{-1} related to $—NH_x$ stretchings indicating a mechanism of NO_x reduction over Pt/AZT which is similar to that of Pt/ZT. We should also note that the formation of $—NH_x$ species, which is an indication of nitrate reduction, occurs at a later time on the Pt/AZT system (Fig. 10a) compared to Pt/ZT (Fig. 9a). This is in very good agreement with the current FTIR and TPD results discussed earlier indicating that nitrate species on the Pt/AZT ternary oxide system possess a higher stability and a higher resilience against reduction with respect to that of the Pt/ZT binary oxide surface. This argument is also in line with the observation that unlike the Pt/ZT binary oxide system (Fig. 9b), no spectral changes were observed for the Pt/AZT ternary oxide surface (Fig. 10b) after 80 min of reduction.

3.4. Monitoring the NO_x reduction products in the gas phase

Gas phase products formed during the NO_x reduction via H_2(g) over Pt/ZT and Pt/AZT surfaces were also monitored by means of gas-phase in situ FTIR spectroscopy. In these set of experiments, catalyst samples were lifted above the IR beam in the spectroscopic reactor, so that the incoming IR photons were only absorbed by the gas phase species. A background spectrum was obtained immediately after the introduction of the H_2(g) into the reactor over the NO_2-saturated catalyst surfaces. All gas-phase in situ FTIR spectra given in Fig. 11 were acquired using the aforementioned background spectra. The evolution of gas-phase reduction products from Pt/ZT and Pt/AZT surfaces over 120 min is shown in Fig. 11a and b, respectively. The gas phase spectra for both materials reveal the immediate formation of N_2O(g) (i.e. 2225 cm^{-1} feature) even after the first minute of H_2(g) exposure, indicating that N_2O is an early intermediate/byproduct of the nitrate reduction mechanism over Pt/ZT and Pt/AZT systems. It is worth mentioning that other possible gas phase reduction features in addition to N_2O(g) such as NH_3(g), was elusive to detect in gas-phase FTIR spectroscopy due to the overwhelming intensity of the H_2O(g) absorption envelope at 1620 cm^{-1} which appeared in the spectra as the IR beam traveled through ambient conditions after exiting the spectroscopic reactor.

4. Conclusions

In the current work, binary and ternary oxide materials, ZrO_2/TiO_2 (ZT) and $Al_2O_3/ZrO_2/TiO_2$ (AZT), as well as their Pt-functionalized counterparts were synthesized by the sol–gel method and characterized by means of XRD, Raman spectroscopy and BET techniques. The NO_x storage capacity (NSC) and reduction performance of each material were investigated and the characteristic behaviors of surface nitrate functional groups upon H_2(g) interaction were monitored via in situ FTIR and TPD analysis. Our findings can be summarized as follows:

- In the ZT binary oxide system, a strong interaction between TiO_2 and ZrO_2 domains were observed at high temperatures (>973 K), which resulted in the formation of a highly ordered crystalline $ZrTiO_4$ phase and a low specific surface area (i.e. 26 m^2/g at 973 K).
- Incorporation of Al_2O_3 in the AZT structure renders the material highly resilient toward crystallization and ordering where AZT material was found to be mostly amorphous even at 1173 K. Moreover, alumina acts as a diffusion barrier in the AZT structure, preventing the formation of $ZrTiO_4$ and leading to a very high specific surface area (i.e. 264 m^2/g at 973 K).
- NO_x adsorption capability of the AZT ternary oxide system was found to be significantly greater than that of ZT, in line with the almost ten-fold greater SSA of the former surface.
- The interaction of NO_2(g) with ZT and AZT surfaces revealed adsorbed nitrate species with similar geometries. While Pt incorporation did not alter the type of the adsorbed nitrate species, it significantly boosted the NO_x adsorption amount on both Pt/ZT and Pt/AZT systems. Thermal stability of nitrates was higher on the AZT compared to ZT, most likely due to the defective structure and the presence of coordinatively unsaturated sites on the former surface.
- Pt sites were found to assist the partial ordering/crystallization of the AZT system. Pt sites were also observed to facilitate the decomposition of nitrates in the absence of an external reducing agent by shifting the decomposition temperatures to lower values and by boosting the formation of N_2 and N_2O.

- In the presence of H_2(g), the complete reduction of surface nitrates was achieved at 623 K on ZT, while this was achieved at 723 K for AZT.
- Nitrate reduction over Pt/ZT and Pt/AZT via H_2(g) under mild conditions initially leads to the conversion of bridging nitrates into monodentate nitrates and nitrites together with the formation of surface —OH and —NH_x functionalities. N_2O(g) was also observed in the very early stages of the reduction process as an initial intermediate/byproduct.

Appendix A. Supplementary data

Supplementary material related to this article can be found, in the online version, at http://dx.doi.org/10.1016/j.cattod.2013.12.037.

References

[1] N. Miyoshi, S. Matsumoto, K. Katoh, T. Tanaka, J. Harada, N. Takahashi, K. Yokota, M. Sugiura, K. Kashahara, SAE Paper 950809, 1995.
[2] N. Takahashi, H. Shinjoh, T. Iijima, T. Suzuki, K. Yamazaki, K. Yokota, H. Suzuki, N. Miyoshi, S. Matsumoto, T. Tanizawa, T. Tanaka, S. Tateishi, K. Kasahara, Catalysis Today 27 (1996) 63.
[3] S. Roy, A. Baiker, Chemical Reviews 109 (2009) 4054.
[4] W.S. Epling, L.E. Campbell, A. Yezerets, N.W. Currier, J.E. Parks, Catalysis Reviews 46 (2004) 163.
[5] E. Ozensoy, J. Szanyi, C.H.F. Peden, Journal of Catalysis 243 (2006) 149.
[6] E.I. Vovk, E. Emmez, M. Erbudak, V.I. Bukhtiyarov, E. Ozensoy, Journal of Physical Chemistry C 115 (2011) 24256.
[7] E.I. Vovk, A. Turksoy, V.I. Bukhtiyarov, E. Ozensoy, Journal of Physical Chemistry C 117 (2013) 7713.
[8] Z. Say, E.I. Vovk, V.I. Bukhtiyarov, E. Ozensoy, Applied Catalysis B: Environmental 142–143 (2013) 89.
[9] R. Hummatov, D. Toffoli, O. Gulseren, E. Ozensoy, H. Ustunel, Journal of Physical Chemistry C 116 (2012) 6191.
[10] Z. Say, E.I. Vovk, V.I. Bukhtiyarov, E. Ozensoy, Topics in Catalysis 56 (2013) 950.
[11] S.M. Andonova, G.S. Senturk, E. Kayhan, E. Ozensoy, Journal of Physical Chemistry C 113 (2009) 11014.
[12] E. Emmez, E.I. Vovk, V.I. Bukhtiyarov, E. Ozensoy, Journal of Physical Chemistry C 115 (2011) 22438.
[13] G.S. Senturk, E.I. Vovk, V.I. Zaikovskii, Z. Say, A.M. Soylu, V.I. Bukhtiyarov, E. Ozensoy, Catalysis Today 184 (2012) 54.
[14] S. Matsumoto, Y. Ikeda, H. Suzuki, M. Ogai, N. Miyoshi, Applied Catalysis B: Environmental 25 (2000) 115.
[15] S.M. Andonova, G.S. Senturk, E. Ozensoy, Journal of Physical Chemistry C 114 (2010) 17003.
[16] T. Kanazawa, Catalysis Today 96 (2004) 171.
[17] K. Ito, S. Kakino, K. Ikeue, M. Machida, Applied Catalysis B: Environmental 74 (2007) 137.
[18] K. Arata, Akutagawa, K. Tanabe, Bulletin of the Chemical Society of Japan 49 (1976) 390.
[19] I. Wang, W.F. Chang, R.J. Shiau, J.C. Wu, C.S. Chung, Journal of Catalysis 83 (1983) 428.
[20] N. Takahashi, A. Suda, I. Hachisuka, M. Sugiura, H. Sobukawa, H. Shinjoh, Applied Catalysis B: Environmental 72 (2007) 187.
[21] H. Imagawa, T. Tanaka, N. Takahashi, S. Matsunaga, A. Suda, H. Shinjoh, Journal of Catalysis 251 (2007) 315.
[22] H. Imagawa, N. Takahashi, T. Tanaka, S. Matsunaga, H. Shinjoh, Applied Catalysis B: Environmental 92 (2009) 23.
[23] M.A. Krebs, R.A. Condrate, Journal of Materials Science Letters 7 (1988) 1327.
[24] F. Azough, R. Freer, J. Petzelt, Journal of Materials Science 28 (1993) 2273.
[25] V. Lughi, D.R. Clarke, Journal of Applied Physics 101 (5) (2007) 053524.
[26] M.T. Colomer, M. Maczka, Journal of Solid State Chemistry 184 (2011) 365.
[27] C.A. Ulin, J.A. de Los Reyes, J. Escobar, M.C. Barrera, M.A. Cortes-Jacome, Journal of Physics and Chemistry of Solids 71 (2010) 1004.
[28] K. Hadjiivanov, V. Bushev, M. Kantcheva, D. Klissurski, Langmuir 10 (1994) 464.
[29] M. Kantcheva, Applied Catalysis B: Environmental 42 (2003) 89.
[30] M. Kantcheva, V.S. Vakkasoglu, Journal of Catalysis 223 (2004) 352.
[31] M. Kantcheva, Journal of Catalysis 204 (2001) 479.
[32] E. Kayhan, S.M. Andonova, G.S. Senturk, C.C. Chusuei, E. Ozensoy, Journal of Physical Chemistry C 114 (2010) 357.
[33] Z. Say, M. Tohumeken, E. Vovk, E. Ozensoy, in preparation.
[34] T. Szailer, J.H. Kwak, D.H. Kim, J.C. Hanson, C.H.F. Peden, J. Szanyi, Journal of Catalysis 239 (2006) 51.
[35] M. Kantcheva, E.Z. Ciftlikli, Journal of Physical Chemistry B 106 (2002) 3941.
[36] K.T. Jung, A.T. Bell, Journal of Molecular Catalysis A 163 (2000) 27.
[37] G. Cerrato, S. Bordiga, S. Barbera, C. Morterra, Applied Surface Science 115 (1997) 53.
[38] E. Ozensoy, D. Herling, J. Szanyi, Catalysis Today 136 (2008) 46.
[39] G. Busca, Catalysis Today 27 (1996) 457.
[40] G. Busca, Catalysis Today 41 (1998) 191.
[41] D. Dautzenberg, H. Knozinger, Journal of Catalysis 33 (1974) 142.
[42] H. Knozinger, K. Kochloefl, W. Meye, Journal of Catalysis 28 (1973) 69.
[43] A. Davydov, Molecular Spectroscopy of Oxide Catalyst Surfaces, Wiley, USA, 2003, pp. 81–83.
[44] T.A. Gordymova, A.A. Davydov, Journal of Applied Spectroscopy 39 (1983) 621.